PAPER

Check for updates

Ligand effects in photoluminescence of copper nanoclusters†

Peiling Du,‡[a] Sachurilatu,‡[a] Wenya Jiang,‡[b] Jianyu Wei, [ID] *[b] Simin Li*[a] and Hui Shen [ID] *[a]

Copper nanoclusters have attracted significant interest in the field of materials science due to their high abundance, complex structure, and unique properties. However, there is a limited amount of research on the relationship between structure and properties. In this study, we synthesized and comprehensively characterized two new Cu_9 nanoclusters, $[Cu_9(PhSe)_6(PPh_2O_2)_3]$ (**Cu₉-1**) and $[Cu_9(CH_3OPhS)_6(PPh_2O_2)_3]$ (**Cu₉-2**), in order to investigate the effect of ligands on photoluminescence. Both clusters have the same metal skeleton and similar distribution of ligands, with the only difference being the surface ligands (PhSe *vs.* CH_3OPhS). Interestingly, the photoluminescence lifetime of **Cu₉-2** was found to be 3.2 times longer than that of **Cu₉-1**. Furthermore, a notable Stokes shift (ST) was observed in the emission spectra of the two clusters. Single-crystal X-ray analysis revealed the formation of hydrogen bonds between neighboring clusters of **Cu₉-2**, which influenced intramolecular interactions. Additionally, the methoxy groups in **Cu₉-2**, acting as conjugated electron donors, promoted intramolecular charge transfer and π–π interaction. This study is expected to inspire further research on surface ligand engineering for controlling the properties of copper nanoclusters beyond photoluminescence.

Introduction

Metal nanoclusters constitute a fascinating class of nano-materials that exhibit unique physicochemical properties.[1–3] Their size range (below 3 nm) positions them between small molecules and traditional nanoparticles. These nanoclusters have exhibited significant potential across a range of applications, including catalysis, sensing, imaging, and biomedical fields, among others.[4–8] They constitute a rapidly evolving and promising domain of research.[4–9] Ligand-stabilized metal nanoclusters are composed of a core of metal atoms encased in ligand molecules, resulting in a core–shell structure that significantly influences the properties of the clusters.[10–13] The metallic core plays a significant role in determining the optical and various physical characteristics of the clusters, whereas the organic ligands are instrumental in influencing solubility and functionality.[14–20] By meticulously selecting and engineering organic ligands, one can effectively manipulate the struc-

tural characteristics of the clusters. This enables a precise modulation of their properties, thereby enhancing their performance across a variety of applications.[21–23]

Copper (Cu) clusters exhibit numerous notable benefits as a novel category of cluster materials, applicable across a range of fields.[24–28] The presence of multiple oxidation states of copper is fundamental to the formation of diverse copper nuclei, which in turn leads to a variety of structural configurations and properties.[29–32] Moreover, the cuprophilic interactions present within copper nanoclusters, as well as the interactions between copper atoms and ligands, play a crucial role in establishing the molecular packing arrangement. This arrangement subsequently affects the luminescent and charge transport characteristics of the materials.[33–36] Furthermore, the capacity to adjust surface ligands offers extensive opportunities for the design and engineering of copper nanoclusters with customized characteristics suitable for diverse applications.[37,38] In this context, there exists a significant interest in acquiring model copper clusters to facilitate the establishment of correlations between their structural characteristics and associated properties.

Herein, two analogous clusters, $[Cu_9(PhSe)_6(PPh_2O_2)_3]$ (**Cu₉-1**) and $[Cu_9(CH_3OPhS)_6(PPh_2O_2)_3]$ (**Cu₉-2**), were developed and employed as a model system to examine the influence of ligands on the photoluminescence properties of copper clusters. Both clusters exhibit an identical metallic core; however, they are distinguished by the ligands utilized, with **Cu₉-1** incor-

[a]*College of Energy Materials and Chemistry, Inner Mongolia University, Hohhot 010021, China. E-mail: siminli@imu.edu.cnshen@imu.edu.cn*

[b]*School of Materials and New Energy, Ningxia University, Yinchuan, Ningxia 750021, China. E-mail: jianyu.wei@nxu.edu.cn*

†Electronic supplementary information (ESI) available. CCDC 2358101 and 2358288. For ESI and crystallographic data in CIF or other electronic format see DOI: https://doi.org/10.1039/d4dt02060j

‡ These authors contribute equally to this work.

porating PhSe⁻ and **Cu₉-2** incorporating MeOPhS⁻. Notably, the photoluminescence lifetime of **Cu₉-2** was measured at 247.7 μs, 3.2 times longer than that of **Cu₉-1**. This observation underscores the substantial impact that ligands have on the phosphorescent properties of copper clusters. Additional characterization indicated that **Cu₉-2** demonstrates intermolecular hydrogen bonding and enhanced π–π interactions, which culminate in a compact and stable structural configuration. These characteristics are instrumental in producing the unique photoluminescence properties observed in **Cu₉-2** in contrast to **Cu₉-1**. This research highlights the significant influence of peripheral ligands on the regulation of intramolecular interactions and intercluster aggregation, which in turn impacts the phosphorescent characteristics.

Results and discussion

Synthesis of $[Cu_9(PhSe)_6(PPh_2O_2)_3]$ (Cu₉-1) and $[Cu_9(CH_3OPhS)_6(PPh_2O_2)_3]$ (Cu₉-2)

Both **Cu₉-1** and **Cu₉-2** were synthesized utilizing a one-pot synthesis approach. In the experimental protocol, $Cu(Ph_2POO)_2$, PPh_4BPh_4, $NaBH_4$ and PhSeH for **Cu₉-1** or MeOPhSH for **Cu₉-2** were dissolved in a solvent mixture comprising methanol and dichloromethane. The resultant mixture was agitated for a duration of three hours at ambient temperature, leading to the development of an orange-coloured solution. Subsequently, this solution underwent centrifugation and diffusion with ether, culminating in the production of orange bulk crystals as the final products (Fig. S1 and S2†).

### Structure analysis and characterization

Initially, the structural characteristics of the two crystals were validated through single-crystal X-ray diffraction (SCXRD) analysis (Fig. S3 and S4†). The findings indicated that crystal **Cu₉-1** is crystallized in the $R3c$ space group of the trigonal system, whereas crystal **Cu₉-2** is classified within the monoclinic system, specifically exhibiting the $I2/a$ space group (Fig. S5 and S6, see Tables S1 and S2† for detailed crystallographic and refinement data). In the crystal structure of **Cu₉-1**, the asymmetric unit comprises two PhSe ligands, one PPh_2O_2 ligand, and three copper (Cu) atoms. As illustrated in Fig. 1, the nanocluster unit is composed of six PhSe ligands, three PPh_2O_2 ligands, and a metal core consisting of nine copper atoms, leading to the molecular formula of $[Cu_9(PhSe)_6(PPh_2O_2)_3]$ (**Cu₉-1**). The absence of counterions within the structure suggests that the cluster is electrically neutral. **Cu₉-2** is synthesized in a manner analogous to **Cu₉-1**, but with the substitution of MeOPhS⁻ for PhSe⁻.

The Cu_9 metal core within **Cu₉-1** is situated at the center of a Cu_3 equilateral triangle (designated as $Cu_{3\text{-centre}}$, indicated in blue in Fig. 2a). The Cu–Cu bond length measures 2.869(2) Å, which is significantly greater than the bond length typically found in metallic copper, which is 2.56 Å. This indicates that the interactions within the Cu_3 triangular core are compara-
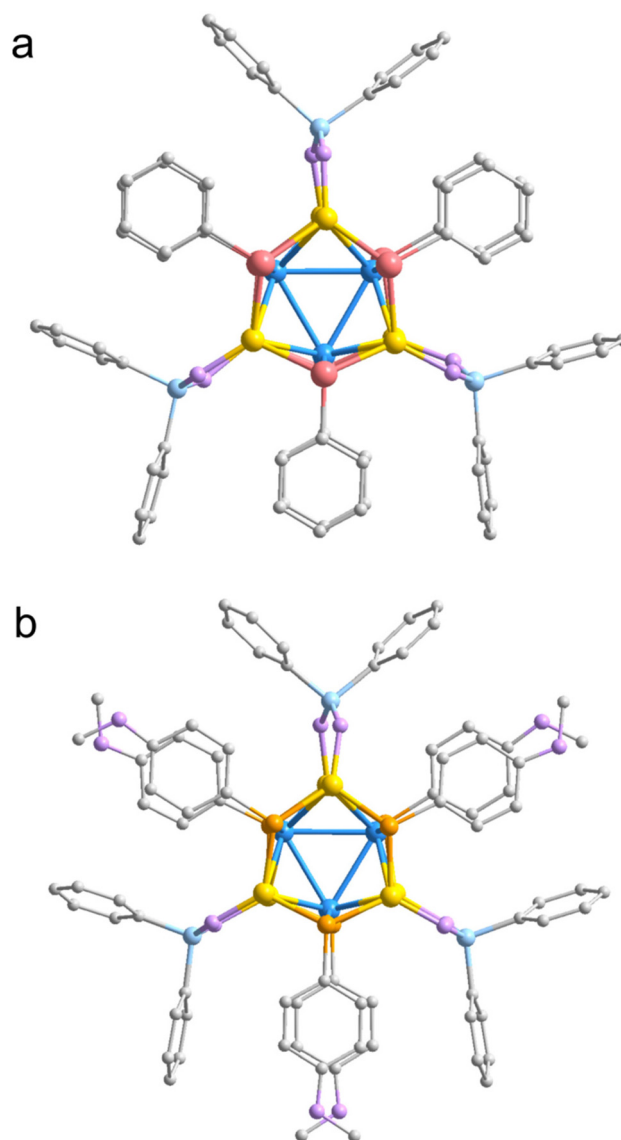
Fig. 1 Total structures of **Cu₉-1** (a) and **Cu₉-2** (b). Colour legend: blue, Cu (centre); yellow, Cu (side); brick red, Se; orange, S; purple, O; light-blue, P; grey, C. All hydrogen atoms are omitted for clarity.

tively weak. The three edges of the $Cu_{3\text{-centre}}$ core rise to create three supplementary triangles, each associated with one of the three Cu atoms positioned above. In this configuration, each edge of the $Cu_{3\text{-centre}}$ core functions as the base for the extended triangles, with the three additional Cu atoms situated at the vertices. The described structure exhibits a crown-like configuration, wherein the $Cu_{3\text{-centre}}$ serves as the base, while the three Cu atoms positioned above it function as the decorative jewels atop the crown (refer to Fig. 2b). The connection of the three peripheral Cu atoms results in the formation of a larger equilateral triangle ($Cu_{3\text{-side}}$, marked in yellow), which is nearly parallel to the $Cu_{3\text{-centre}}$ but oriented in the opposite direction. The elongated Cu–Cu bond length of 4.208 Å on the $Cu_{3\text{-side}}$ necessitates the interconnection of the
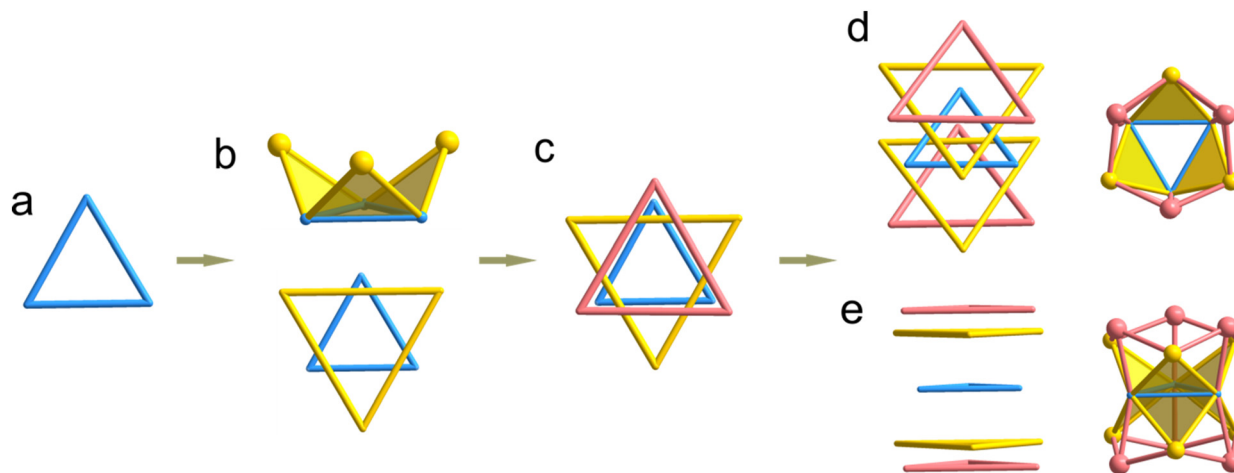
Fig. 2 Core structure of **Cu$_9$-1**. (a) Cu$_{3\text{-centre}}$. (b) Cu$_{3\text{-centre}}$@Cu$_{3\text{-side}}$. (c) Cu$_{3\text{-centre}}$@Cu$_{3\text{-side}}$@Se$_3$. (d) Se$_3$@Cu$_{3\text{-side}}$@Cu$_{3\text{-centre}}$@Se$_3$ viewed from the front. (e) Se$_3$@Cu$_{3\text{-side}}$@Cu$_{3\text{-centre}}$@Se$_3$ viewed from the top. Colour legend: blue, Cu (centre); yellow, Cu (side); brick red, Se.

Cu$_{3\text{-side}}$ that are connected by three Se atoms from PhSe, thereby establishing a "6-crown-3" configuration (Fig. 2d).

The triangular configuration created by the interconnection of the three Se atoms (Se$_3$, with a Se–Se bond length of 3.697 Å, represented in purple in Fig. 2c) is oriented in the same direction as the Cu$_{3\text{-centre}}$. Furthermore, the plane of this triangle is positioned marginally above that of the Cu$_{3\text{-side}}$. In addition, by extending the Cu$_{3\text{-centre}}$ in a downward direction, it is possible to achieve an additional perfectly symmetrical "6-crown-3" configuration. Notably, the upper and lower "6-crown-3" configurations exhibit a near-exact overlap almost exactly along the *c*-axis. Consequently, the Cu$_9$ core of **Cu$_9$-1** is comprised of a Cu$_{3\text{-centre}}$ triangle formed by three copper (Cu) atoms, flanked by two additional Cu$_{3\text{-side}}$ triangles at the upper and lower positions. Additionally, two selenium (Se) triangles are positioned to cap the Cu$_9$ core on both the upper and lower sides. The arrangement of these components from various perspectives is illustrated in Fig. 2d and e, respectively. The three PPh$_2$O$_2$ molecules provide additional stabilization to the Cu$_9$ core by linking the respective vertices of the two Cu$_{3\text{-side}}$ triangles. The bond lengths between the Cu$_{\text{centre}}$ and Cu$_{\text{side}}$ range from 2.667 to 2.717 Å (average: 2.684 Å), which are shorter than those observed in the Cu$_3$ triangle core, but comparable to the Cu–Cu distances found in the complex [Cu$_{13}$\{S$_2$CN^{n}Bu$_2$\}$_6$\{C≡CC(O) OMe\}$_4$]$^+$ (2.522(4) to 2.786(3) Å).[39] This suggests that the interactions among copper atoms are strengthened as one moves from the central region to the peripheral areas. The mean bond length among all Cu atoms is 2.722 Å. The Cu–Se bond distances range from 2.326 Å to 2.428 Å, with an average value of 2.370 Å, which are common in other reported Cu clusters, such as [Cu$_{23}$(PhSe)$_{16}$(Ph$_3$P)$_8$(H)$_6$]·BF$_4$ ($d_{\text{Cu–Se}}$ range: 2.335 to 2.593 Å).[39] The average Cu–O bond distance is 1.932 Å.

Cu$_9$-2 demonstrates a structural resemblance to **Cu$_9$-1**, differing primarily in the substitution of PhSe$^-$ with MeOPhS$^-$ (Fig. S7†). The Cu$_{3\text{-centre}}$ in **Cu$_9$-2** is configured in an isosceles triangular formation, characterized by a waist length of 2.864 Å

and a base length of 2.939 Å. The average bond length between the Cu$_{3\text{-centre}}$ and the Cu$_{\text{side}}$ atoms is 2.656 Å. The bond lengths between the Cu atoms range from 2.584 Å to 2.939 Å, with an average of 2.702 Å. In contrast, the Cu–S bond lengths range from 2.201 Å to 2.297 Å, with an average of 2.251 Å. Additionally, the average Cu–O bond distance is 1.947 Å. It is thus apparent that the average Cu–Cu bond lengths in **Cu$_9$-2** are shorter than those in **Cu$_9$-1**, and similarly, the average Cu–S bond lengths in **Cu$_9$-2** are also reduced compared to those in **Cu$_9$-1**. As a result, **Cu$_9$-2** exhibits a more compact structural configuration.

Furthermore, **Cu$_9$-1** and **Cu$_9$-2** exhibit restricted solubility in a range of organic solvents, such as methanol, ethanol, dichloromethane, trichloromethane, acetonitrile, acetone, and tetrahydrofuran. This presents difficulties in precisely assessing their mass spectrometric characteristics. To mitigate this issue, we performed powder X-ray diffraction (PXRD) analysis to confirm the purity of the compounds. Fig. S8† presents the experimental powder X-ray diffraction (PXRD) patterns for **Cu$_9$-1** and **Cu$_9$-2**, which exhibit a strong correlation with the simulated patterns. Additionally, the X-ray photoelectron spectroscopy (XPS) analysis at the Cu 2p core level identifies two prominent signals at 934.6 and 954.2 eV, corresponding to the Cu 2p$_{3/2}$ and Cu 2p$_{1/2}$, respectively. These signals suggest the existence of Cu atoms with a +1 oxidation state within the Cu$_9$ clusters (see Fig. S9†).

Photoluminescence (PL) properties

The photoluminescence (PL) characteristics of the clusters **Cu$_9$-1** and **Cu$_9$-2** were subsequently investigated. At a temperature of 298 K, the excitation spectra for both **Cu$_9$-1** and **Cu$_9$-2** exhibited similarities when subjected to excitation by light at approximately 466 nm. **Cu$_9$-1** demonstrated photoluminescence (PL) at approximately 648 nm, accompanied by a shoulder feature near 684 nm, and exhibited an absolute photoluminescence quantum yield (PLQY) of approximately 0.36% in air. **Cu$_9$-2** also exhibited PL at approximately 648 nm,

accompanied by a shoulder feature near 680 nm (Fig. S10†). The absolute PLQY of **Cu₉-2** in air was approximately 0.63%. Both **Cu₉-1** and **Cu₉-2** demonstrated dual emission characteristics, accompanied by a notable Stokes shift (ST).[40,41] The PL lifetimes (τ) of **Cu₉-1** and **Cu₉-2** at a temperature of 298 K were recorded at 16.4 μs and 18.6 μs, respectively, suggesting the presence of phosphorescent emission (Fig. S11†).[42]

Subsequently, the photoluminescence characteristics of the **Cu₉-1** and **Cu₉-2** clusters were evaluated at a temperature of 77 K. At this temperature, **Cu₉-1** exhibited emission at a wavelength of 660 nm, accompanied by a shoulder at 675 nm, whereas **Cu₉-2** demonstrated emission at a wavelength of 718 nm. The findings indicate that **Cu₉-2** exhibits a larger Stokes shift, attributed to the π–π interactions and intramolecular charge transfer (refer to Fig. 3a and b). The temperature-dependent luminescence characteristics of the solid-state samples were assessed over a range from 303 K to 83 K, revealing distinct luminescent behaviors for both clusters at lower temperatures. Notably, as the temperature was reduced from 303 K to 83 K, there was a significant increase in both the intensity and lifetime of the phosphorescence. Specifically, **Cu₉-1** demonstrated a redshift of 11 nm, with an enhancement factor of 5.4 (Fig. S12†). In contrast, **Cu₉-2** exhibited a more substantial redshift of 27 nm, accompanied by an enhancement factor of 10.6 (illustrated in Fig. 3c). The larger red shifts transitioning from 303 K to 83 K suggest a greater energy gap between the singlet (S1) and triplet (T1) states in **Cu₉-2**. Previous research has established that the singlet and triplet

energy gap (ΔE_{ST}) significantly influence the light lifetime, efficiency, and color characteristics of luminescent materials.[43,44] Materials with a larger ΔE_{ST} are likely to display enhanced luminous color contrast and a larger Stokes shift, which is beneficial for achieving emissions at longer wavelengths. This study substantiates that the emission wavelength of **Cu₉-2** surpasses that of **Cu₉-1**.

Upon a reduction in temperature to 77 K, the PL lifetime (τ) of **Cu₉-1** and **Cu₉-2** was prolonged by 78.1 μs and 247.7 μs, respectively. Furthermore, **Cu₉-2** exhibited an exceptionally extended lifetime (see Fig. 3d). This phenomenon can be explained by the progressive enhancement of hydrogen bonds and π–π interactions in **Cu₉-2** as the temperature decreases. As a result, the decay rate of phosphorescent radiation, denoted as k_p, exhibited a reduction, which in turn enhanced luminous efficiency and extended the duration of luminous life. Additionally, there was a decrease in the mobility of the cluster, which served to impede the non-radiative transitions of the triplet excitons.

To gain insight into the different photoluminescent characteristics of the two clusters, we conducted a thorough structural analysis. As shown in Fig. S13,† both **Cu₉-1** and **Cu₉-2** display three pairs of nearly parallel benzene rings, which can be attributed to π–π interactions. The densely packed configuration of molecules, characterized by a significant presence of π-conjugated chromophores and short-range π–π interactions, serves to effectively suppress non-radiative transitions, consequently extending the lifetime of the phosphor. The inter-ring distances between the benzene rings in **Cu₉-2** are 3.579 Å, 3.741 Å, and 3.744 Å, respectively, which are notably smaller than the uniform distance of 3.896 Å (see Fig. S13†). This reduction in distance suggests a stronger π–π interaction within **Cu₉-2**. The enhanced π–π interactions present in **Cu₉-2** contribute to a further decrease in the energies of the highest occupied molecular orbital (HOMO) and the lowest unoccupied molecular orbital (LUMO). In such a system, π-electrons are not merely localized between two carbon atoms; rather, they can be distributed across multiple atoms. This electron delocalization results in an expansion of the electron cloud, which in turn lowers the overall energy of the system. More specifically, orbital overlap between conjugated (pi) components facilitates the formation of new molecular orbitals (MOs). These newly formed MOs are capable of more effectively dispersing the electron density and are energetically closer together, thereby diminishing the HOMO–LUMO energy gap. This reduction in the energy gap has implications not only for the electron transfer characteristics of the molecule but also for its optical properties, leading to red shifts in optical emission spectra.

Furthermore, **Cu₉-2** is characterized by the presence of a methoxy group (MeOPh) attached to each of its six benzene rings. The lone pair of electrons in methoxy engages in conjugation with the π-electron system of the aromatic ring. These methoxy groups function as conjugated electron donors, facilitating the charge transfer (CT) process from the outside to the inside and enhancing the electron delocalization within the system. This leads to a decrease in the energy gap between the ground state and the excited state, causing the emitted light to
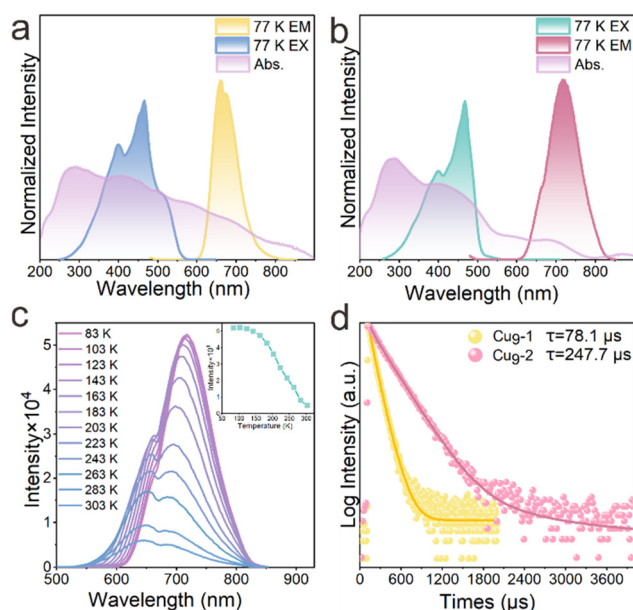
Fig. 3 (a) Excitation (blue, λ_{em} = 466 nm), emission (yellow) and solid-state UV-Vis absorption (purple) spectra of **Cu₉-1** at 77 K. (b) Excitation (green, λ_{em} = 467 nm), emission (red) and solid-state UV-Vis absorption (purple) spectra of **Cu₉-2** at 77 K. (c) Temperature dependence of the emission spectra in the range of 83–303 K of **Cu₉-2**. Insert: maximum photoluminescence intensity at each temperature. (d) Plots of emission decay lifetime of **Cu₉-1** and of **Cu₉-2** at 77 K.
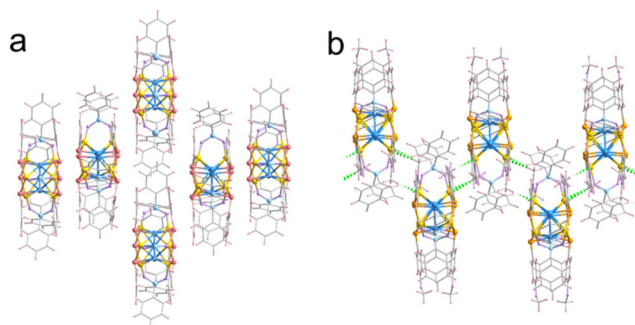
Fig. 4 The packing structures of **Cu$_9$-1** (a) and **Cu$_9$-2** (b). Colour legend: blue, Cu (centre); yellow, Cu (side); brick red, Se; orange, S; purple, O; light-blue, P; grey, C; pink, H. Hydrogen bonding between Cu and H: green.

have lower energy and a longer wavelength, which may cause the large Stokes shift.[45,46]

More surprisingly, the stacking configuration of the cluster **Cu$_9$-2**, as depicted in Fig. 4b, demonstrates a distinctive arrangement characterized by a reverse and alternating stacking pattern. This exceptional structural organization arises from the interaction of two copper atoms on two Cu$_{3-sides}$ of each cluster, which are linked to adjacent clusters *via* hydrogen bonding interactions. It facilitates the formation of a network in which multiple clusters are interconnected in an alternating manner, resulting in a dense and stable configuration. The hydrogen bonding interactions present among the clusters in **Cu$_9$-2** not only bolster the stability of the stacking arrangement, but also augment the overall cohesion and intercluster interactions, thereby enhancing the electronic and optical properties of the cluster **Cu$_9$-2** assembly. In contrast, **Cu$_9$-1** does not exhibit a comparable hydrogen bonding structure (see Fig. 4a).

In **Cu$_9$-2**, the methoxy groups function as conjugated electron donors, facilitating intramolecular charge transfer and enhancing electron delocalization, establishing hydrogen bonding between neighboring clusters. This interaction results in a notable increase in the phosphorescence lifetime at low temperatures, an enhancement in luminous efficiency, and the attainment of longer wavelength emission relative to **Cu$_9$-1**. In other words, the presence of MeOPhS$^-$ is essential for the emission of phosphorescence, significantly prolonging the phosphorescence lifetime at low temperatures, enhancing luminous efficiency, and facilitating emission at longer wavelengths. This insight into the conformational relationships of the clusters enhances our understanding and application of ligand-functionalized clusters, thereby aiding in the future rational design of such clusters.

Conclusions

In conclusion, we synthesized two Cu$_9$ nanoclusters with an identical metal core and tailorable ligands. **Cu$_9$-1** was stabil-

ized by PhSe$^-$ ligands, while **Cu$_9$-2** by MeOPhS$^-$. By introducing different ligands, the formation of hydrogen bonds between neighboring clusters of **Cu$_9$-2** has been shown to influence intramolecular interactions and intermetallic aggregation within the cluster assembly. Moreover, the methoxy groups in **Cu$_9$-2**, as conjugated electron donors, promote intramolecular charge transfer and π–π interaction. This contributes to greatly extending the low-temperature phosphorescence life, improving the luminous efficiency, and achieving longer wavelength emission of the cluster compared to **Cu$_9$-1**. This structural modification opens up new possibilities for designing and engineering copper clusters with improved optical properties for various applications in luminescent materials.

Experimental

Materials

Diphenylphosphinic acid (Ph$_2$POOH, 98%), sodium borohydride (NaBH$_4$, 98%) and 4-methoxythiophenol (MeOC$_6$H$_5$SH, 97%) were purchased from Bidepharm (Shanghai, China). Tetraphenylphosphonium tetraphenylborate (PPh$_4$BPh$_4$, 98%) was purchased from TCI (Tianjin). Benzeneselenol (C$_6$H$_5$SeH, 90%) was purchased from HEWNS (Tianjin). Cu(NO$_3$)$_2$·3H$_2$O (AR) was purchased from Tianjin Fengchuan Chemical Reagent Co., Ltd (Tianjin, China). Acetonitrile (CH$_3$CN, A.R.), hexane (C$_6$H$_{14}$, A.R.), dichloromethane (CH$_2$Cl$_2$, A.R.), methanol (CH$_3$OH, A.R.) and ether (C$_4$H$_{10}$O, A.R.) were purchased from Sinopharm Chemical Reagent Co. Ltd (Shanghai, China). Water used in all experiments was ultrapure. All other reagents were used as received without further purification.

Synthesis

General synthetic process of Cu(Ph$_2$POO)$_2$. To a methanolic solution of Cu(NO$_3$)$_2$·3H$_2$O (1.0 mmol in 10 ml methanol), a solution of Ph$_2$POOH (1.0 mmol in 10 ml acetonitrile) was added under stirring. The stirring was continued for 2 days. Single crystals of Cu(Ph$_2$POO)$_2$ were obtained by slow evaporation of the solvents. Single crystals were filtered, washed with hexane and dried.

General synthetic process of Cu$_9$-1 and Cu$_9$-2. 50 mg (0.1 mmol) Cu(Ph$_2$POO)$_2$, 20 mg (0.03 mmol) PPh$_4$BPh$_4$, 3.8 mg (0.025 mmol, for **Cu$_9$-1**) C$_6$H$_5$SeH or 6.8 mg MeOPhSH (0.05 mmol, for **Cu$_9$-2**) and 40 mg NaBH$_4$ were dissolved in a mixed solvent of 1 mL methanol and 3 mL dichloromethane. The mixture was stirred at room temperature over a period of 3 h, resulting in an orange solution. Orange block crystals were obtained by vapor diffusion of ether into the solution. 6.9% yield for **Cu$_9$-1** and 14.2% yield for **Cu$_9$-2** (based on Cu).

Characterizations

PXRD. The powder X-ray diffraction (PXRD) spectra were recorded by a Bruker AFS D8 ADVANCE. The X-ray photoelectron spectroscopic (XPS) data were collected on ESCALABXI + System (Thermo Fisher Scientific, U.K). The C 1s peak of

adventitious carbon was used for position correction (284.5 eV) in all cases. Luminescence, lifetime and quantum yields were measured by Edinburgh FLS-1000 spectrometer.

Crystallography. The diffraction data of the single crystals of **Cu₉-1** and **Cu₉-2** was collected on an Agilent Technologies SuperNova system X-ray single-crystal diffractometer using Cu Kα (λ = 1.54184 Å) at 100 K. The data were processed using CrysAlis^{Pro}. The structure was solved and refined using full-matrix least-squares based on F^2 using ShelXT,[47] ShelXL[48] in Olex2.[49] The thermal ellipsoids of the ORTEP diagram were done at 50% probability. Detailed crystal data and structure refinements for the compound are given in Tables S1 and S2.† The CCDC number 2358288 (**Cu₉-1**) and 2358101 (**Cu₉-2**)† contain the supplementary crystallographic data for this study.

Author contributions

PD, Saqorrltu, WJ and SL performed the experiments under the guidance of JW and HS. The data were analysed by PD, SL, and HS. The manuscript was written by PD, SL and verified by HS.

Data availability

CCDC number 2358288 (**Cu₉-1**) and 2358101 (**Cu₉-2**) contain the supplementary crystallographic data for this study.

Conflicts of interest

There are no conflicts to declare.

Acknowledgements

References

1 I. Chakraborty and T. Pradeep, Atomically Precise Clusters of Noble Metals: Emerging Link between Atoms and Nanoparticles, *Chem. Rev.*, 2017, **117**, 8208–8271.

2 R. Jin, C. Zeng, M. Zhou and Y. Chen, Atomically Precise Colloidal Metal Nanoclusters and Nanoparticles: Fundamentals and Opportunities, *Chem. Rev.*, 2016, **116**, 10346–10413.

3 M. Matus and H. Häkkinen, Understanding ligand-protected noble metal nanoclusters at work, *Nat. Rev. Mater.*, 2023, **8**, 372–389.

4 X. X. Xu, Y. Liu, F. Sun, Y. Y. Jia, Q. H. Xu, J. Q. Tang, Z. L. Xie, J. Sun, S. M. Li, Q. Tang, S. Guo, H. Shen and N. F. Zheng, Array-Based Clusters of Copper with Largely Exposed Metal Sites for Promoting Catalysis, *Chem. Mater.*, 2023, **35**, 7588–7596.

5 T. Imaoka, Y. Akanuma, N. Haruta, S. Tsuchiya, K. Ishihara, T. Okayasu, W. J. Chun, M. Takahashi and K. Yamamoto, Platinum clusters with precise numbers of atoms for preparative-scale catalysis, *Nat. Commun.*, 2017, **8**, 688.

6 R. W. Huang, Y. S. Wei, X. Y. Dong, X. Wu, C. X. Du, S. Q. Zang and T. C. W. Mak, Hypersensitive dual-function luminescence switching of a silver-chalcogenolate cluster-based metal–organic framework, *Nat. Chem.*, 2017, **9**, 689–697.

7 D. C. Lim, B. Y. Seo, S. G. Nho, D. H. Kim, E. M. Hong, J. Y. Lee, S. Y. Park, C. L. Lee, Y. D. Kim and S. Cho, Emissive Nanoclusters Based on Subnanometer–Sized Au₃₈ Cores for Boosting the Performance of Inverted Organic Photovoltaic Cells, *Adv. Energy Mater.*, 2015, **5**, 1500393.

8 H. Shen, Q. Y. Wu, S. Malola, Y. Z. Han, Z. Xu, R. Qin, X. K. Tang, Y. Chen, B. K. Teo, H. Häkkinen and N. F. Zheng, N-Heterocyclic Carbene-Stabilized Gold Nanoclusters with Organometallic Motifs for Promoting Catalysis, *J. Am. Chem. Soc.*, 2022, **144**, 10844–10853.

9 W. Qiao, Y. Wang, S. Li, R. Wang, J. Wu and S. Q. Zang, Integrating Homogeneous and Heterogeneous Catalysis in a Copper Nanocluster with Lewis Acid–Base Sites for Chemical Conversion of CO₂ and Propargylamine, *CCS Chem.*, 2024, 1–11.

10 K. Konishi, M. Iwasaki and Y. Shichibu, Phosphine-Ligated Gold Clusters with Core + exo Geometries: Unique Properties and Interactions at the Ligand-Cluster Interface, *Acc. Chem. Res.*, 2018, **51**, 3125–3133.

11 P. N. Gunawardene, J. L. Martin, J. M. Wong, Z. F. Ding, J. F. Corrigan and M. S. Workentin, Controlling the Structure, Properties and Surface Reactivity of Clickable Azide–Functionalized Au₂₅(SR)₁₈ Nanocluster Platforms Through Regioisomeric Ligand Modifications, *Angew. Chem., Int. Ed.*, 2022, **61**, e202205194.

12 Z. Qin, S. Sharma, C. Wan, S. Malola, W. Xu, H. Häkkinen and G. Li, A Homoleptic Alkynyl-Ligated [Au₁₃Ag₁₆L₂₄]³⁻ Cluster as a Catalytically Active Eight-Electron Superatom, *Angew. Chem., Int. Ed.*, 2021, **60**, 970–975.

13 C. Dong, R. W. Huang, C. Chen, J. Chen, S. Nematulloev, X. Guo, A. Ghosh, B. Alamer, M. N. Hedhili, T. T. Isimjan, Y. Han, O. F. Mohammed and O. M. Bakr, [Cu₃₆H₁₀(PET)₂₄(PPh₃)₆Cl₂] Reveals Surface Vacancy Defects in Ligand-Stabilized Metal Nanoclusters, *J. Am. Chem. Soc.*, 2021, **143**, 11026–11035.

14 S. Sharma, K. K. Chakrahari, J. Saillard and C. W. Liu, Structurally Precise Dichalcogenolate-Protected Copper and Silver Superatomic Nanoclusters and Their Alloys, *Acc. Chem. Res.*, 2018, **51**, 2475–2483.

15 Q. Yao, T. Chen, X. Yuan and J. Xie, Toward Total Synthesis of Thiolate-Protected Metal Nanoclusters, *Acc. Chem. Res.*, 2018, **51**, 1338–1348.

16 K. Isozaki, R. Ueno, K. Ishibashi, G. Nakano, H. Z. Yin, K. Iseri, M. Sakamoto, H. Takaya, T. Teranishi and M. Nakamura, Gold Nanocluster Functionalized with Peptide Dendron Thiolates: Acceleration of the Photocatalytic Oxidation of an Amino Alcohol in a Supramolecular Reaction Field, *ACS Catal.*, 2021, **11**, 13180–13187.

17 S. Chandra, Nonappa, G. Beaune, A. Som, S. Zhou, J. Lahtinen, H. Jiang, J. V. I. Timonen, O. Ikkala and R. H. A. Ras, Highly Luminescent Gold Nanocluster Frameworks, *Adv. Opt. Mater.*, 2019, **7**, 1900620.

18 L. B. Qin, F. Sun, X. S. Ma, G. Y. Ma, Y. Tang, L. K. Wang, Q. Tang, R. C. Jin and Z. H. Tang, Homoleptic Alkynyl-Protected Ag_{15} Nanocluster with Atomic Precision: Structural Analysis and Electrocatalytic Performance toward CO_2 Reduction, *Angew. Chem., Int. Ed.*, 2021, **60**, 26136–26141.

19 Q. You, X. L. Jiang, W. T. Fan, Y. S. Cui, Y. Zhao, S. L. Zhuang, W. M. Gu, L. W. Liao, C. Q. Xu, J. Li and Z. Wu, Pd_8 Nanocluster with Nonmetal-to-Metal-Ring Coordination and Promising Photothermal Conversion Efficiency, *Angew. Chem., Int. Ed.*, 2024, **63**, e202313491.

20 C. Zhang, Z. Wang, W. Si, L. Wang, J. Dou, Z. Gao, C. Tung and D. Sun, Solvent-Induced Isomeric Cu_{13} Nanoclusters: Chlorine to Copper Charge Transfer Boosting Molecular Oxygen Activation in Sulfide Selective Oxidation, *ACS Nano*, 2022, **16**, 9598–9607.

21 L. Jin, D. S. Weinberger, M. Melaimi, C. E. Moore, A. L. Rheingold and G. Bertrand, Trinuclear gold clusters supported by cyclic (alkyl)(amino)carbene ligands: mimics for gold heterogeneous catalysts, *Angew. Chem., Int. Ed.*, 2014, **53**, 9059–9063.

22 T. D. Nguyen, Z. R. Jones, D. F. Leto, G. A. Wu, S. L. Scott and T. W. Hayton, Ligand-Exchange-Induced Growth of an Atomically Precise Cu_{29} Nanocluster from a Smaller Cluster, *Chem. Mater.*, 2016, **28**, 8385–8390.

23 X. J. Wang, B. Yin, L. R. Jiang, C. Yang, Y. Liu, G. Zou, S. Chen and M. Zhu, Ligand-protected metal nanoclusters as low-loss, highly polarized emitters for optical wave-guides, *Science*, 2024, **381**, 784–790.

24 A. Baghdasaryan and T. Bürgi, Copper nanoclusters: designed synthesis, structural diversity, and multiplatform applications, *Nanoscale*, 2021, **13**, 6283–6340.

25 B. Han, Z. Liu, L. Feng, Z. Wang, R. K. Gupta, C. M. Aikens, C. Tung and D. Sun, Polymorphism in Atomically Precise Cu_{23} Nanocluster Incorporating Tetrahedral $[Cu_4]^0$ Kernel, *J. Am. Chem. Soc.*, 2020, **142**, 5834–5841.

26 T. D. Nguyen, Z. R. Jones, B. R. Goldsmith, W. R. Buratto, G. Wu, S. L. Scott and T. W. Hayton, A Cu_{25} Nanocluster with Partial Cu(0) Character, *J. Am. Chem. Soc.*, 2015, **137**, 13319–13324.

27 G. Yang, Y. Xie, Y. Wang, Y. Tang, L. L. Chng, F. Jiang, F. Du, X. Zhou, J. Y. Ying and X. Yuan, Water-soluble Cu_{30} nanoclusters as a click chemistry catalyst for living cell labeling via azide-alkyne cycloaddition, *Nano Res.*, 2023, **16**, 1748–1754.

28 Y. Yun, L. Li, M. Zhou, M. Li, N. Sun, H. Li, S. Jin, C. Zuo, H. Sheng and M. Zhu, Atomically precise coreless AuCu bimetallic nanoclusters for Ullmann C-O coupling, *Nano Res.*, 2023, **16**, 10756–10762.

29 Y. M. Wang, X. C. Lin, K. M. Mo, M. Xie, Y. L. Huang, G. H. Ning and D. Li, An Atomically Precise Pyrazolate–Protected Copper Nanocluster Exhibiting Exceptional Stability and Catalytic Activity, *Angew. Chem., Int. Ed.*, 2023, **62**, e202218369.

30 C. Xu, Y. H. Jin, H. Fang, H. J. Zheng, J. C. Carozza, Y. X. Pan, P. J. Wei, Z. Y. Zhang, Z. Wei, Z. Zhou and H. X. Han, A High-Nuclearity Copper Sulfide Nanocluster $[S-Cu_{50}]$ Featuring a Double-Shell Structure Configuration with Cu(II)/Cu(I) Valences, *J. Am. Chem. Soc.*, 2023, **145**, 25673–25685.

31 J. Sun, X. D. Yan, L. Z. Wang, Z. L. Xie, G. L. Tian, L. Wang, A. He, S. M. Li, Q. X. Guo, Chaolumen, J. L. He and H. Shen, Decorating an Anticuboctahedral Copper Kernel with Labile Surface Coatings for Controlling Optical and Catalytic Properties, *Inorg. Chem.*, 2023, **62**, 9005–9013.

32 H. Wu, G. N. Andrew, R. Anumula and Z. Luo, How ligand coordination and superatomic-states accommodate the structure and property of a metal cluster: $Cu_4(dppy)_4Cl_2$ vs. $Cu_{21}(dppy)_{10}$ with altered photoluminescence, *Chin. Chem. Lett.*, 2024, **35**, 108340.

33 Y. Zhang, Z. D. Lu, A. R. Feng, J. W. Y. Lam, Z. G. Wang, Y. E. Shi and B. Z. Tang, Green–Emissive Copper Nanocluster with Aggregation–Enhanced Emission for Selective Detection of Al^{3+}, *Chem. – Eur. J.*, 2023, **29**, e202203554.

34 R. S. Dhayal, J. Liao, Y. Lin, P. Liao, S. Kahlal, J. Saillard and C. W. Liu, A Nanospheric Polyhydrido Copper Cluster of Elongated Triangular Orthobicupola Array: Liberation of H_2 from Solar Energy, *J. Am. Chem. Soc.*, 2013, **135**, 4704–4707.

35 X. Fan, F. Yuan, J. Wang, Z. Cheng, S. Xiang, H. Yang and Z. Zhang, Structural Isomerization in Cu(I) Clusters: Tracing the Cu Thermal Migration Paths and Unveiling the Structure-Dependent Photoluminescence, *CCS Chem.*, 2022, **5**, 350–360.

36 C. Deng, B. Han, Z. Liu, Z. Pan, J. He, Y. Li, Z. Yang, G. Luo, C. Tung, D. Sun and L. Zheng, Hierarchical Homochiral Assembly of Polyhedral Cage-Type Nanoclusters, *CCS Chem.*, 2024, 1–12.

37 K. Basu, S. Paul, R. Jana, A. Datta and A. Banerjee, Red-Emitting Copper Nanoclusters: From Bulk-Scale Synthesis to Catalytic Reduction, *ACS Sustainable Chem. Eng.*, 2019, **7**, 1998–2007.

38 L. Liu, Z. Wang, Z. Wang, R. Wang, S. Q. Zang and T. C. W. Mak, Mediating CO_2 Electroreduction Activity and Selectivity over Atomically Precise Copper Clusters, *Angew. Chem., Int. Ed.*, 2022, **61**, e202205626.

39 R. W. Huang, J. Yin, C. Dong, P. Maity, M. N. Hedhili, S. Nematulloev, B. Alamer, A. Ghosh, O. F. Mohammed and

O. M. Bakr, [Cu$_{23}$(PhSe)$_{16}$(Ph$_3$P)$_8$(H)$_6$]·BF$_4$: Atomic-Level Insights into Cuboidal Polyhydrido Copper Nanoclusters and Their Quasi-simple Cubic Self-Assembly, *ACS Mater. Lett.*, 2021, **3**, 90–99.

40 S. Havenridge and C. M. Aikens, Deciphering the dual emission in the photoluminescence of Au$_{14}$Cd(SR)$_{12}$: A theoretical study using TDDFT and TDDFT + TB, *J. Chem. Phys.*, 2021, **155**, 074302.

41 L. Luo, Z. Liu, X. Du and R. Jin, Near-Infrared Dual Emission from the Au$_{42}$(SR)$_{32}$ Nanocluster and Tailoring of Intersystem Crossing, *J. Am. Chem. Soc.*, 2022, **144**, 19243–19247.

42 W. Q. Shi, L. L. Zeng, R. L. He, X. S. Han, Z. J. Guan, M. Zhou and Q. M. Wang, Near-unity NIR phosphorescent quantum yield from a room-temperature solvated metal nanocluster, *Science*, 2024, **383**, 326–330.

43 P. Chandrashekar, G. Sardar, T. Sengupta, A. C. Reber, P. K. Mondal, D. Kabra, S. N. Khanna, P. Deria and S. Mandal, Modulation of Singlet-Triplet Gap in Atomically Precise Silver Cluster-Assembled Material, *Angew. Chem., Int. Ed.*, 2024, **63**, e202317345.

44 W. Si, C. Zhang, M. Zhou, W. Tian, Z. Wang, Q. Hu, K. Song, L. Feng, X. Huang, Z. Gao, C. Tung and D. Sun, Two triplet emitting states in one emitter: Near-infrared dual-phosphorescent Au$_{20}$ nanocluster, *Sci. Adv.*, 2023, **9**, eadg3587.

45 L. Wang, Z. Xiong, J. Zhi Sun, F. Huang, H. Zhang and B. Z. Tang, How the Length of Through-Space Conjugation Influences the Clusteroluminescence of Oligo(Phenylene Methylene)s, *Angew. Chem., Int. Ed.*, 2024, **63**, e202318245.

46 J. Zhang, Y. Tu, H. Shen, J. W. Y. Lam, J. Sun, H. Zhang and B. Z. Tang, Regulating the proximity effect of heterocycle-containing AIEgens, *Nat. Commun.*, 2023, **14**, 3772.

47 G. M. Sheldrick, SHELXT-integrated space-group and crystal-structure determination, *Acta Crystallogr., Sect. A: Found. Adv.*, 2015, **71**, 3–8.

48 C. B. Hubschle, G. M. Sheldrick and B. Dittrich, ShelXle: a Qt graphical user interface for SHELXL, *J. Appl. Crystallogr.*, 2011, **44**, 1281–1284.

49 O. V. Dolomanov, L. J. Bourhis, R. J. Gildea, J. A. K. Howard and H. Puschmann, OLEX2: a complete structure solution, refinement and analysis program, *J. Appl. Crystallogr.*, 2009, **42**, 339–341.